Photoexcited Electrons Driven by Doping Concentration Gradient: Flux-Prepared NaTaO3 Photocatalysts Doped with Strontium Cations

An, Longjie ; Kitta, Mitsunori ; Iwase, Akihide ; Kudo, Akihiko ; Ichikuni, Nobuyuki ; Onishi, Hiroshi

(Citation)
ACS Catalysis,8(10):9334-9341

(Issue Date)
2018-10

(Resource Type)
journal article

(Version)
Version of Record

ACS Catalysis

Research Article

Cite This: ACS Catal. 2018, 8, 9334−9341

pubs.acs.org/acscatalysis

Photoexcited Electrons Driven by Doping Concentration Gradient: Flux-Prepared $NaTaO_3$ Photocatalysts Doped with Strontium Cations

Longjie An,[†] Mitsunori Kitta,[‡] Akihide Iwase,[§] Akihiko Kudo,[§] Nobuyuki Ichikuni,[∥] and Hiroshi Onishi*[,†]

[†]Department of Chemistry, Graduate School of Science, Kobe University, Nada, Kobe, Hyogo 657-8501, Japan

[‡]Research Institute for Ubiquitous Energy Devices, National Institute of Advanced Industrial Science and Technology, Midorigaoka, Ikeda, Osaka 563-8577, Japan

[§]Department of Applied Chemistry, Faculty of Science, Tokyo University of Science, Kagurazaka, Shinjuku, Tokyo 162-8601, Japan

[∥]Department of Applied Chemistry and Biotechnology, Graduate School of Engineering, Chiba University, Inage, Chiba 263-8522, Japan

Supporting Information

ABSTRACT: Electron−hole recombination always competes with desired reactions on semiconductor photocatalysts. Reducing recombination probability is essential for increasing the quantum efficiency of the reactions. Previous studies demonstrated that doping with lanthanoid or alkaline-earth metal cations reduced recombination probability in $NaTaO_3$ photocatalysts for artificial photosynthesis. The motivation behind this study was to reveal how the guest metal cations reduced recombination probability. $NaTaO_3$ photocatalysts were doped with Sr cations through crystallization in molten NaCl flux to produce 50−100 nm sized particles of $NaTaO_3$−$Sr(Sr_{1/3}Ta_{2/3})O_3$ solid solution. Intraparticle distribution of Sr cations was sensitive to immersion time in the hot flux with a fixed Sr concentration of 2 mol % relative to Ta. Extended immersion for 60 h resulted in a homogeneous Sr distribution. Curtailed immersion for 1 h yielded particles capped with a 3 nm thick Sr-accumulated layer. The population of electrons bandgap-excited under Hg−Xe lamp irradiation was enhanced in the 1-h immersed photocatalyst by 160 times relative to that in a Sr-free $NaTaO_3$ photocatalyst. In the 60-h immersed photocatalyst, population enhancement was not more than 9 times. We interpreted the large population enhancement in the 1-h immersed photocatalyst with a concentration gradient of Sr cations from the surface to bulk. The concentration gradient induced an energy gradient of conduction-band minimum. Photoexcited electrons were driven on the energy gradient to be separated from holes. The overall water splitting reaction rate was evaluated on the photocatalysts to show a 4-times enhancement on the 1-h immersed photocatalyst relative to the rate on the Sr-free photocatalyst. The reaction-rate enhancement less than the electron population enhancement was ascribed to a limited fraction of electrons overriding the energy gradient and returning back to the surface.

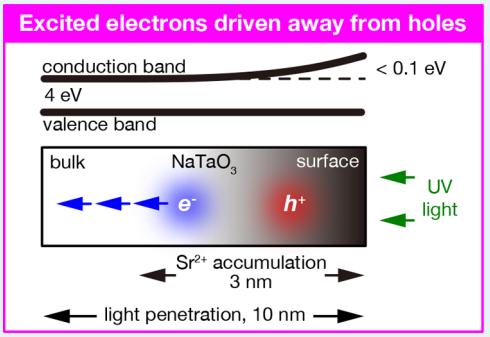

KEYWORDS: *photocatalysis, electron−hole recombination, perovskite structure, solid solution, solar energy conversion*

1. INTRODUCTION

Visible-light sensitivity and high quantum efficiency are simultaneously required to achieve artificial photosynthesis on a practical scale. Single-element doping has been frequently used to sensitize wide-bandgap semiconductors to visible light. Multielement doping facilitated by solid solution formation has further been examined,[1−8] where cation and anion charges were balanced with no need to create ion vacancies. A recent study[9] demonstrated $LaTaON_2$−$La(Mg_{2/3}Ta_{1/3})O_3$ solid solutions operable at 600 nm for photocatalytic overall water splitting. However, quantum efficiency was still limited to 0.03% at 440 nm. Electron−hole recombination enhanced by doping can be a major reason for the limited efficiency, since guest elements can result in impurities in the host semiconductor crystals.

Kudo and co-workers found a route to avoid doping-induced recombination. They developed $NaTaO_3$ photocatalysts doped with lanthanoid[10,11] or alkaline-earth metal[12−14] cations. Apparent quantum efficiency for the overall water splitting reaction *increased* to 50% or more by doping with the metal cations. Onishi and co-workers[15,16] then showed electron−hole recombination that was limited by doping La^{3+}, Ca^{2+}, Sr^{2+}, or Ba^{2+} cations. Their recent studies[17−19] were focused on Sr-

Received: June 23, 2018
Revised: August 26, 2018
Published: August 27, 2018

doped $NaTaO_3$ to reveal formation of $NaTaO_3$−Sr-$(Sr_{1/3}Ta_{2/3})O_3$ solid solutions. This solid solution is recognized as $NaTaO_3$ doubly doped with one element; A-site cations (Na^+) and B-site cations (Ta^{5+}) in the perovskite-structured lattice are simultaneously doped with Sr^{2+} cations. They further proposed that the electron−hole recombination rate is controlled by the Sr concentration gradient in photocatalyst particles. A gradient from Sr-rich surface to Sr-poor core was spontaneously created in photocatalyst preparation through the solid-state reaction. The concentration gradient of the Sr cations occupying the B site induced the energy gradient of conduction-band minimum. Bandgap-excited electrons were driven by the energy gradient to be separated from holes.

The motivation behind the present study was to test this hypothesis for increasing excited electron population and thus photocatalytic activity. The wide bandgap of $NaTaO_3$ (4 eV) limits the viability of this particular compound for artificial photosynthesis. However, an efficient scheme of doping, once established in $NaTaO_3$, can be applied to a broad range of solid-solution photocatalysts intentionally equipped with composition gradient.

Photocatalysts doped with Sr cations were prepared in molten NaCl flux. Extended immersion for 60 h in the hot flux yielded photocatalyst particles with a homogeneous Sr distribution. Curtailed immersion for 1 h produced particles capped with a 3 nm thick, Sr-accumulated layer. By capping with the accumulated layer, the electron population excited under Hg−Xe lamp irradiation was enhanced by 160 times relative to the population in Sr-free $NaTaO_3$. Population enhancement remained 9 times higher in the 60-h immersed photocatalyst with the homogeneous Sr distribution. The population enhancement sensitive to the presence or absence of the Sr-accumulated surface layer, which should have produced a concentration gradient of Sr cations, as expected on the hypothesis.

2. EXPERIMENTAL SECTION

2.1. Photocatalysts Preparation. Strontium-doped $NaTaO_3$ photocatalysts, hereafter referred to as Sr-NTO, were prepared in NaCl flux. Crystallization in molten flux is a useful method for preparing particles[20−25] and films[26,27] of $NaTaO_3$ and related materials functional in photocatalysis.

Na_2CO_3 (99.8%, Kanto), Ta_2O_5 (99.99%, Rare Metallic) and $SrCO_3$ (99.9%, Kanto) were mixed with NaCl (99.5%, Wako). The Sr/Ta ratio in the mixture was adjusted to 2 mol % with a Na_2CO_3/Ta_2O_5 molar ratio of 1.05. A fraction of NaCl flux was set at 50 wt % relative to the mixture. The mixture was placed in four alumina crucibles and heated at 1423 K for 1, 10, 20, or 60 h to produce photocatalysts with different immersion times, 1h-Sr-NTO, 10h-Sr-NTO, and so on. Another mixture without $SrCO_3$ was heated at 1423 K for 10 h to produce Sr-free $NaTaO_3$, NTO. The heated mixtures were washed with water to remove excess NaCl. Sr-NTOs thereby prepared were chemically etched when necessary. Sr-NTO photocatalysts to be etched (0.25 g) were stirred in an aqueous HF solution (10 wt %, Wako) of 3 mL for 10 min at room temperature and then washed with water until the pH of the washing fluid was maintained at 7.

2.2. Photocatalysts Characterization. The chemical composition and crystallographic phase of the prepared photocatalysts were checked with an energy dispersive X-ray fluorescence spectrometer (Shimadzu, EDX-720) and an X-ray diffractometer (Rigaku, SmartLab). The size and shape of particles were evaluated by a scanning electron microscope (Hitachi High-Technologies, S-4800). Light absorption spectra of the photocatalysts were observed with a spectrometer (Jasco, V-570) equipped with an integration sphere. Raman scattering was observed in air using a spectrometer (Jasco, NRS-7100) with an excitation wavelength of 532 nm. X-ray absorption spectra of 10h-Sr-NTO were determined in BL-12C of Photon Factory with a Si(111) double crystal monochromator. An ion chamber with a half mixture of Ar and N_2 was used to detect incident X-ray intensity. Sr *K* edge absorption spectra were accumulated in the fluorescence mode using a 19-element solid-state detector. Energy dispersive X-ray mapping was conducted in a transmission electron microscope (FEI, TITAN^3 G2 60−300) equipped with a Si drift detector (FEI, super-X) and imaging software (Bruker, Esprit).

Infrared light absorption induced by ultraviolet (UV) light irradiation was observed to evaluate the steady-state population of photoexcited electrons that had not yet recombined. Photocatalyst particles were suspended in water to a weight concentration of 3 g L^{-1}. 0.5 mL of the suspension was transferred to a CaF_2 plate and dried at room temperature for 20 h in air. The transmission IR absorption spectrum of the dried plate was obtained under a vacuum of 10 Pa with a Fourier-transform spectrometer (Jasco, FT/IR610) in the presence and absence of UV light irradiation provided by a 200-W Hg−Xe lamp (San-ei Electric, UVS-204S). Light power at wavelengths of shorter than 370 nm was 60 mW cm^{-2} in the full spectrum of radiation. The rate of overall water splitting reaction was determined with photocatalyst of 0.5 g suspended in pure water and irradiated with a 400 W high-pressure Hg lamp. Evolved H_2 and O_2 were quantified by gas chromatography.

3. RESULTS AND DISCUSSION

3.1. Chemical Composition. Bulk composition of 1h-Sr-NTO, 10h-Sr-NTO, 20h-Sr-NTO, and 60h-Sr-NTO was examined. X-ray fluorescence results are summarized in Figure 1. Sr Kα spectra of the four Sr-NTOs were identical as shown in panel (A). The integrated intensity of the Sr Kα emission was normalized to that of Ta Lα emission to evaluate the Sr/Ta molar ratio. The evaluated ratio fell in a narrow range of 2.0 ± 0.1 mol % indicating that the Sr concentration was insensitive to heating time. Strontium cations in the starting material were fully incorporated into the calcined photocatalysts.

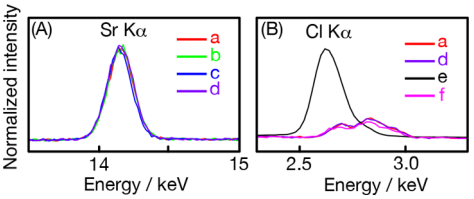

Figure 1. X-ray fluorescence spectra of Sr-NTOs. Panel A shows the Sr Kα spectra of (a): 1h-Sr-NTO, (b) 10h-Sr-NTO, (c) 20h-Sr-NTO, and (d) 60h-Sr-NTO. Panel B presents spectra appearing in the energy range of 2.3−3.3 keV. Spectrum e was observed on NaCl. A Sr-free $NaTaO_3$ photocatalyst synthesized via the solid-state method presented spectrum f. Signal intensity was normalized to that of Ta Lα emission in each object other than NaCl.

Another issue to be examined is possible contamination of Cl from the flux. Cl Kα emission would appear at 2.6 keV, if

DOI: 10.1021/acscatal.8b02437
ACS Catal. 2018, 8, 9334−9341

contaminated. As recognized in two representative spectra of 1h-Sr-NTO and 60h-Sr-NTO, which are shown in panel B, weak signals appeared at 2.70, 2.83, and 2.95 keV. The triple-peaked spectrum disagreed with Cl Kα emission of NaCl with one major peak at 2.62 keV. Hence the absence of Cl was concluded in our photocatalysts. A Sr-free $NaTaO_3$ prepared through the solid-state method, where $NaCO_3$ and Ta_2O_5 were heated at 1173 K for 1 h and then 1423 K for 10 h in the absence of the flux, presented the triple-peaked spectrum. This supports Cl-free composition of Sr-NTOs, since the solid-state prepared $NaTaO_3$ has no chance of Cl contamination.

3.2. Crystallographic Phase. A single perovskite-structured phase was checked and confirmed by X-ray diffraction. Figure 2A shows diffraction patterns of the flux-prepared Sr-

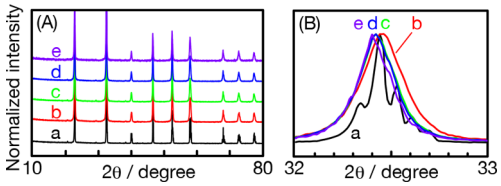

Figure 2. X-ray diffraction patterns of (a) NTO, (b) 1h-Sr-NTO, (c) 10h-Sr-NTO, (d) 20h-Sr-NTO, and (e) 60h-Sr-NTO. Panel A shows peaks in the range 10−80° and panel B presents shifts of the peak at 32.4−32.5°. Diffraction patterns in parts A and B are normalized to that peak.

NTOs and NTO. The peak position and relative intensity of diffraction peaks were similar on the five photocatalysts and consistent with the diffraction patterns of perovskite-structured $NaTaO_3$ observed in earlier studies.[28]

Shifts of the peak at 2θ = 32.4−32.5° are shown in panel B. 1h-Sr-NTO presented a broadened peak with no shift from the peak of NTO. The broadened diffraction suggests a reduced size of the photocatalyst particles, which is confirmed with scanning electron micrographs in the following subsection. Uneven Sr distribution in the particles should also have induced inhomogeneous lattice spacings to broaden diffraction. By extending immersion time to 10, 20, and 60 h, the peak became less broadened. It is natural that extended immersion induced more homogenized composition and homogeneous lattice spacings in each particle.

The center of the peak slightly shifted to low angles in peaks c, d, and e, suggesting lattice expansion. Lattice expansion induced by doping with Sr cations is not surprising. Our earlier study[19] evidenced $NaTaO_3$−$Sr(Sr_{1/3}Ta_{2/3})O_3$ solid solutions formed by doping thorough the solid-state method. In the solid solutions, a finite fraction of Ta^{5+} at B sites in the perovskite-structured lattice was doped with Sr^{2+} in spite of their different ionic radii, 0.06 nm of Ta^{5+} and 0.12 nm of Sr^{2+}.[29] Doping small Ta^{5+} with large Sr^{2+} caused the lattice to expand.

3.3. Particle Shape. Figure 3 shows scanning electron micrographs of the flux-prepared photocatalysts. Micrometer-sized cubic primary particles with round corners were produced in the absence of Sr (image a). The size of the primary particles was reduced to 50−100 nm by doping at 2 mol % while insensitive to immersion time (images b−e).

One characteristic feature is the smooth surface of Sr-NTO particles. When $NaTaO_3$ was doped with Sr cations through the solid-state reaction, regularly separated ten-nanometer-length steps appeared over the particle surface.[14] The surface restructuring with regular steps was later interpreted with

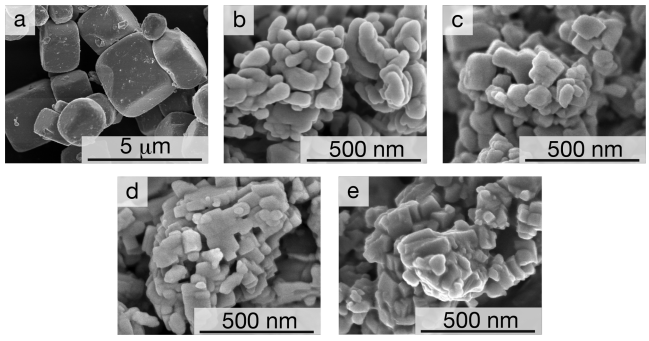

Figure 3. Scanning electron micrographs of (a) NTO, (b) 1h-Sr-NTO, (c) 10h-Sr-NTO, (d) 20h-Sr-NTO, and (e) 60h-Sr-NTO.

core−shell structured solid solution.[17] A Sr-rich shell formed in a heteroepitaxial manner over a Sr-poor core. The regularly separated steps spontaneously appeared to correct the lattice mismatch at core−shell boundaries. The smoothly truncated particles suggested lattice mismatch insufficient to induce surface restructuring on the flux-prepared Sr-NTO particles.

3.4. Elemental Mapping. Figure 4 shows a set of scanning transmission electron microscope (STEM) images of 1h-Sr-NTO. A particle with a side length of 150 nm was present in the center of the annular dark field image shown in panel a. The upper corner of the particle is zoomed to recognize Ta atom columns in panel b. Lattice distortion with twins or dislocations is absent to indicate a well-crystallized character of the particle even doped with Sr cations.

A set of element maps were acquired in a portion marked with the square in image a. The principal elements, Ta, O and Na, presented homogeneous distributions from the bulk to the surface of the particle, as depicted in the four panels in part c. Strontium exhibited an inhomogeneous distribution with an accumulated layer capping the surface, in contrast to the principal elements. The thickness of the Sr-accumulated layer was 3 nm as deduced in the line profiles d. Energy dispersive X-ray spectra observed in and out of the accumulated layer are available in Supporting Information (Figure S1).

The extensively immersed photocatalyst, 60h-Sr-NTO, was similarly characterized, and it presented a homogeneous Sr distribution. A set of element maps with line profiles are shown in Figure S2. The Sr-accumulated layer was present on 1h-Sr-NTO and absent on 60h-Sr-NTO. This set of results indicates that the homogeneous distribution is thermodynamically favorable, while surface accumulation of Sr cations is kinetically favorable. When Na_2O (produced from $NaCO_3$), Ta_2O_5, and SrO are completely dissolved in NaCl flux at 1423 K, and Sr-containing $NaTaO_3$ is crystallized during cooling, we find no reason to produce 1h-Sr-NTO and 60h-Sr-NTO with different Sr distributions. It is suspect that SrO solid particles remain in the hot flux, while the other two oxides are dissolved and produce Sr-free $NaTaO_3$ particles. This is a reasonable conclusion since the melting point of SrO (2804 K)[30] is higher than those of Na_2O (1407 K),[30] Ta_2O_5 (2148 K),[30] and $NaTaO_3$ (2083 K).[31] Strontium cations then transport from solid SrO to $NaTaO_3$ particles through the flux. The Sr-accumulated layer was thereby produced on the surface of 1h-Sr-NTO particles. When SrO solid is exhausted in the crucible, the one-way transport of Sr cations is complete, and Sr distribution starts to be homogenized in each particle. In a similar manner, Sr cations are expected to be accumulated on

DOI: 10.1021/acscatal.8b02437
ACS Catal. 2018, 8, 9334−9341

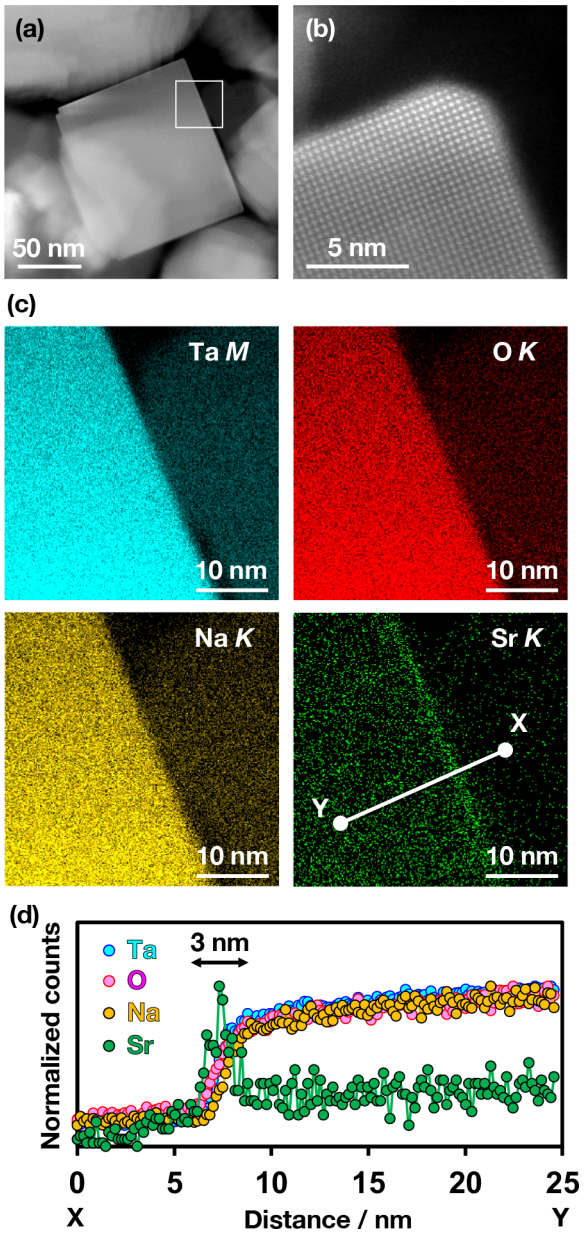

Figure 4. Scanning transmission electron micrographs of 1h-Sr-NTO. (a) Annular dark field image of particles. (b) Ta atom columns in a particle. (c) Element maps obtained with Ta *M*, O *K*, Na *K*, and Sr *K* emissions. The analyzed portion is marked with the white square in part a. (d) X-ray count profiles along line *X*–*Y*.

the surface of 10h-Sr-NTO and 20h-Sr-NTO according to the immersion time between the two extremes, 1 and 60 h.

3.5. Raman Scattering. We interpreted the low-angle shifts of the diffraction peak with B-site doping in 3.2. Raman spectra of the photocatalysts are shown in Figure 5 to support B-site doping in Sr-NTOs. Three bands at 450, 500, and 620 cm^{-1} are attributed to Raman-active lattice vibration of the $NaTaO_3$ host lattice.[32] The four Sr-NTOs exhibited an additional band at 860 cm^{-1}. In our earlier study,[17] the 860 cm^{-1} band was assigned to the breathing vibration of TaO_6 octahedra in $NaTaO_3$–$Sr(Sr_{1/3}Ta_{2/3})O_3$ solid solution. This mode of vibration possesses A_{1g} symmetry and cannot contribute to Raman scattering in a cubic, perovskite-structured lattice because of symmetry restriction. In the solid solution, TaO_6 octahedra lose the cubic symmetry to

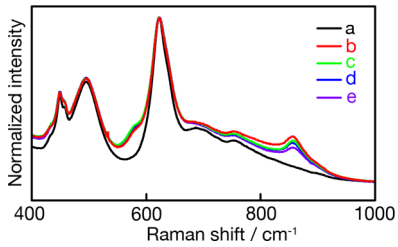

Figure 5. Raman spectra of the flux-prepared photocatalysts: (a) NTO, (b) 1h-Sr-NTO, (c) 10h-Sr-NTO, (d) 20h-Sr-NTO, and (e) 60h-Sr-NTO. Intensity was normalized at 620 cm^{-1}.

produce the 860 cm^{-1} band when neighbored by SrO_6 octahedra. Hence the 860 cm^{-1}-band in spectra a–d was evidence of B-site doping in Sr-NTOs.

The 860 cm^{-1} band gradually weakened with immersion time from 1 to 60 h. This suggests a reduced number of Sr cations at B sites with immersion time, since 860 cm^{-1} band intensity was nearly proportional to Sr concentration in Sr-doped $NaTaO_3$ prepared through the solid-state method.[17] We assumed that extended immersion produced a homogeneous and stoichiometric $NaTaO_3$–$Sr(Sr_{1/3}Ta_{2/3})O_3$ solid solution. The 860 cm^{-1} band strengthened in 1h-Sr-NTO suggested a larger number of Sr cations occupying the B site than expected in the stoichiometric solid solution. Strontium concentration averaged over particles remained as 2.0 ± 0.1 mol % regardless of immersion time as described in 3.1. To accommodate more Sr cations at the B site, the composition of the solid solution should deviate from the stoichiometry.

3.6. X-ray Absorption. The local environment of Sr cations accommodated in 10h-Sr-NTO was examined with extended X-ray absorption fine structure (EXAFS) at the Sr *K* edge. The k^3-weighted absorption spectrum observed at 3–11 $Å^{-1}$ is shown in Figure 6a. For reference, the spectrum of a Sr-

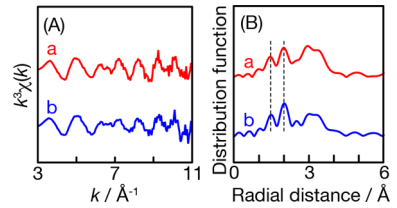

Figure 6. Extended X-ray absorption fine structure at Sr *K* edge. (A) k^3-weighted absorption spectrum and (B) radial distribution function. (a) 10h-Sr-NTO and (b) Sr-doped $NaTaO_3$ photocatalyst prepared through the solid-state method.[19] Distribution peaking at 1.4 and 2.0 Å is marked with broken lines. The *k* range in Fourier transform was 3–11 $Å^{-1}$.

doped $NaTaO_3$ photocatalyst (Sr concentration: 2.1 mol %) prepared through the solid-state reaction is shown together, which the authors previously reported.[19] The two k^3-weighted spectra were identical. The radial distribution functions, which were given by Fourier transform of the k^3-weighted spectra, were hence identical. These results indicate the local environment of Sr cations were identical in the two photocatalysts prepared in the different methods.

In the solid-state prepared photocatalyst,[19] two Sr–O shells were observed. One small shell with a Sr–O length of 1.96 Å corresponds to SrO_6 octahedra with Sr cations occupying the B site, Sr(B). The other large shell with a Sr–O length of 2.60 Å corresponds to SrO_{12} cuboctahedra with Sr cations at the A

DOI: 10.1021/acscatal.8b02437
ACS Catal. 2018, 8, 9334–9341

site, Sr(A). The radial distribution functions shown in Figure 6B peaked at 1.4 and 2.0 Å corresponding to the small and large shells, respectively. The apparently reduced Sr−O lengths were caused by phase shifts in electron scattering. This assignment of Sr−O shells confirmed the formation of a $NaTaO_3$−$Sr(Sr_{1/3}Ta_{2/3})O_3$ solid solution in 10h-Sr-NTO. Additional peaks at 2.5−3.5 Å in the radial distribution functions were ascribed to Sr(A)−Ta and Sr(B)−Na shells.

The near-edge structure (XANES) of 10h-Sr-NTO and the solid-state prepared photocatalyst are shown in Figure S3. They are identical with each other being consistent with the EXAFS results.

3.7. Photoexcited Electron Population. The steady-state population of photoexcited electrons was enhanced by doping with Sr cations. Figure 7(A) shows the change in the IR

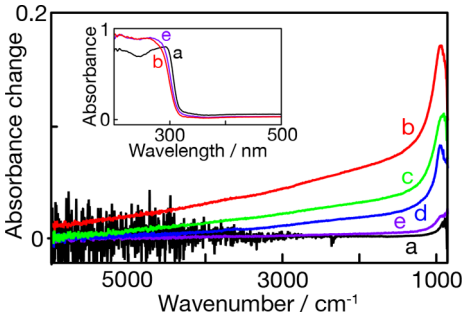

Figure 7. IR absorption change induced by UV light irradiation: (a) NTO, (b) 1h-Sr-NTO, (c) 10h-Sr-NTO, (d) 20h-Sr-NTO, and (e) 60h-Sr-NTO. UV light absorption spectra of parts a, b, and e are shown in the inset.

absorbance spectra induced by UV light irradiation. The four Sr-NTOs and NTO presented positive absorbance-changes increased monotonically with decreasing wavenumber from 6000 to 900 cm^{-1}. This monotonic IR absorption spectrum was assigned to excitation of bandgap-excited electrons not yet recombined, following earlier studies conducted on Ta-containing photocatalysts, $NaTaO_3$[15−17] and $K_3Ta_3B_2O_{12}$.[33]

Absorbance change was integrated in the range of 6000−900 cm^{-1} to quantify the steady-state population of photoexcited electrons. Absorbance change was most enhanced on 1h-Sr-NTO. The enhancement relative to the absorbance change of NTO was 160 times. Electron−hole recombination was limited in 1h-Sr-NTO accordingly. Infrared absorption was observed on photocatalysts placed in the vacuum, where surface reactions consuming photoexcited electrons or holes were absent. The rate of electron−hole recombination was balanced with the rate of electron−hole excitation. In the weak excitation extreme, where one electron and one hole are excited in one particle, the recombination rate is proportional to the population of electrons not yet recombined. The first-order rate constant of recombination is inversely proportional to the steady-state population of excited electrons detected by IR absorption.

Doping with Sr^{2+} cations in NaCl flux effectively increased electron population as has been achieved by doping through the solid-state reaction. With the solid-state reaction, a maximum enhancement of 180 times was observed at a Sr concentration of 1.8 mol %.[17] Doping in the flux as well as in the solid-state reaction provided population enhancements by more than 2 orders of magnitude. Doping via the hydrothermal reaction, by contrast, caused no population enhancement.[17]

The important issue here is IR absorbance-change sensitivity to immersion time in the flux. Integrated absorbance change decreased from 160 on 1h-Sr-NTO to 75 on 10h-Sr-NTO, 43 on 20h-Sr-NTO, and eventually 9 on 60h-Sr-NTO, in the unit of the absorbance change on NTO. Absorbance change in 60h-Sr-NTO was smaller by 17 times than that in 1h-Sr-NTO. This systematic reduction demonstrates excited electron population sensitive to immersion time, i.e., sensitive to how Sr cations are distributed in each particle. Particle-averaged Sr concentration was insensitive to immersion time (Figure 1). Single perovskite-structured phase was always present (Figure 2) with B-site doping with Sr cations (Figures 5 and 6). The size of the particles was unchanged with extended immersion (Figure 3). As shown in the inset of Figure 7, 1h-Sr-NTO and 60h-Sr-NTO presented almost identical UV absorption spectra indicating a fixed rate of excitation under lamp irradiation. These properties cannot contribute to the electron population sensitive to immersion time. Instead, elemental mapping with STEM revealed a Sr-accumulated layer capping 1h-Sr-NTO particles (Figure 4), which was absent on 60h-Sr-NTO.

The thickness of the accumulated layer was 3 nm. It may be surprising that the single-nanometer scale architecture on 50−100 nm sized particles enhanced the excited electron population by more than 2 orders of magnitude. However, the layer thickness was compatible to the penetration depth of excitation light. The light source, a Hg−Xe lamp, provided intense radiation at 254 nm. This wavelength is in the absorption spectrum of bandgap excitation away from the absorption edge. With photon energies sufficiently greater than the bandgap energy of a semiconductor, electrons are directly excited from the valence band to the conduction band with no change in momentum. Absorption coefficient increases to the order of 10^8 m^{-1} at these photon energies.[34] The penetration depth at 254 nm is hence estimated to be on the order of 10 nm, though the absolute number of the absorption coefficient is unknown on $NaTaO_3$. Electrons and holes were created in or near the accumulated layer where the number of Sr cations occupying the B site was reduced from the surface to bulk.

In the $NaTaO_3$−$Sr(Sr_{1/3}Ta_{2/3})O_3$ solid solution, SrO_6 octahedra are embedded in the network of the TaO_6 octahedra by doping. The embedded SrO_6 octahedra hinder the overlap of the Ta 5d orbitals, which narrows the conduction band with the upward shift of the band minimum. The concentration gradient of the Sr cations induces the energy gradient of the conduction band minimum. Bandgap-excited electrons are driven by the energy gradient to be separated from the complementary holes. We now apply this hypothesis to the Sr-accumulated layer on 1h-Sr-NTO as illustrated in the TOC graphic. The hypothesized upward shift of the conduction band minimum was estimated to be 0.1 eV or less. The absorption edge shifted by 5−10 nm on Sr-NTOs relative to Sr-free NTO according to the UV absorption spectra as shown in the inset of Figure 7. An absorption edge shift by 10 at 300 nm represents a bandgap broadened by 0.1 eV.

3.8. Response to HF Etching. Two photocatalysts, 1h-Sr-NTO and 60h-Sr-NTO, were chemically etched in the HF solution for 10 min at room temperature to further support the key role of the Sr-accumulated layer. The 3 nm thick layer of 1h-Sr-NTO should have been removed by etching, whereas 60h-Sr-NTO with the homogeneous Sr distribution experienced no change other than reducing particle size. Photoexcited electron population are expected to be sensitive to etching on 1h-Sr-NTO and insensitive on 60-Sr-NTO.

DOI: 10.1021/acscatal.8b02437
ACS Catal. 2018, 8, 9334−9341

Etched 1h-Sr-NTO is characterized as shown in Figure 8. Sr *Kα* fluorescent X-ray intensity decreased by 6% and the 860

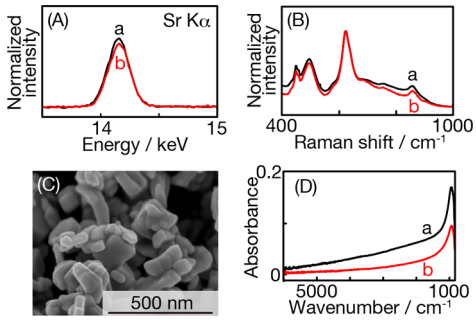

Figure 8. 1h-Sr-NTO etched with the HF solution. (A) X-ray fluorescence spectra of (a) unetched and (b) etched photocatalysts. Intensity was normalized to that of Ta *Lα* emission. (B) Raman spectra of (a) unetched and (b) etched photocatalysts. Intensity was normalized at 620 cm^{-1}. (C) Scanning electron micrograph of the etched photocatalyst. (D) IR absorbance change induced by UV-light irradiation on (a) unetched and (b) etched photocatalysts.

cm^{-1} band in Raman scattering weakened, as shown in panels A and B. Fluorescent X-ray and Raman scattering are bulk-sensitive probes to quantify particle-averaged concentration of total Sr cations and Sr cations placed at B sites, respectively. The decreased signals provide a sign of the Sr-accumulated layer removed by etching. Size change of photocatalyst particles was not recognized in the scanning electron micrograph (panel C). Steady-state population of electrons excited by lamp irradiation was reduced as expected. Panel D presents UV-induced IR absorbance change before and after etching. Integrated absorbance change decreased from 160 (unetched) to 65 (etched), in the unit of the absorbance change on NTO, to demonstrate that photoexcited electron population was reduced by 60%.

60h-Sr-NTO was etched and characterized for reference. X-ray fluorescence, Raman scattering and scanning electron micrograph (Figure 9) were unchanged by etching. This is because Sr cations were homogeneously distributed in particles. Etching produced particles slightly smaller (not detectable in the micrograph) than the originals with Sr distribution unchanged. The steady-state population of photo-

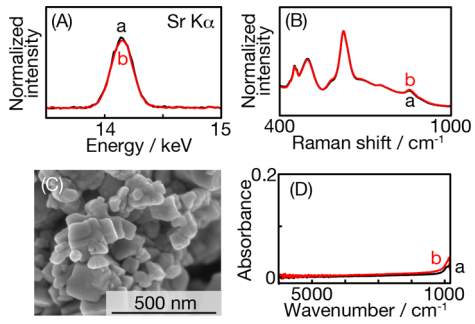

Figure 9. 60h-Sr-NTO etched with the HF solution. (A) X-ray fluorescence spectra of (a) unetched and (b) etched photocatalysts. Intensity was normalized to that of Ta-*Lα* emission. (B) Raman spectra of (a) unetched and (b) etched photocatalysts. Intensity was normalized at 620 cm^{-1}. (C) Scanning electron micrograph of etched photocatalyst. (D) IR absorbance change induced by UV-light irradiation on (a) unetched and (b) etched photocatalysts.

excited electrons, which was quantified by integrated IR absorbance change, changed only slightly from 9 (unetched) to 17 (etched). The absolute decrease from 160 to 65 on etched 1h-Sr-NTO was much larger than the absolute increase on etched 60h-Sr-NTO. These observations support the scheme of electron population controlled by the presence or absence of the Sr-accumulated layer on photocatalyst particles.

3.9. Water Splitting Activity. Water splitting activity was finally evaluated by detecting H_2 and O_2 produced under UV light irradiation from a Hg-lamp of 400 W in the absence of cocatalyst. The amount of gas production is plotted in Figure S4 as a function of irradiation time up to 16 h. The gas-production rate was deduced from the figures and summarized in Table 1. Sr-free NTO showed the lowest production rates.

Table 1. H_2 and O_2 Production of the Flux-Prepared Photocatalysts[a]

Photocatalyst	Production rate/μmol h^{-1}		
	H_2	O_2	H_2/O_2 ratio
NTO	11	2.8	3.9
1h-Sr-NTO	39	13	3.0
10h-Sr-NTO	55	22	2.5
20h-Sr-NTO	123	52	2.4
60h-Sr-NTO	44	16	2.8
La-doped $NaTaO_3$	392	183	2.1

[a]Cocatalyst was not loaded. The rates on a solid-state prepared $NaTaO_3$ doped with La cations at 2 mol % are shown for reference.

Rates on Sr-NTOs increased with immersion time in the order of 1, 10, 20 h and decreased on 60h-Sr-NTO. 20h-Sr-NTO was most active H_2 and O_2 production rates enhanced by 11 and 19 times relative to those on the Sr-free NTO. The absolute rate on 20h-Sr-NTO was 31% (H_2) and 28% (O_2) of that observed on a solid-state prepared $NaTaO_3$ doped with La cations at 2 mol % as a reference.

Here we consider the relationship of gas production rates and photoexcited electron population. Electron population was quantified in a vacuum by integrating IR absorbance change (Figure 7). An equal number of holes should have been present in the photocatalyst, though the holes were invisible in IR absorption. Figure 10 shows gas production rates of the five flux-prepared photocatalysts as a function of integrated IR absorbance change, i.e., the population of electrons or holes. Two Sr-containing photocatalysts (60h-Sr-NTO and 20h-Sr-NTO) exhibited production rates nearly proportional to

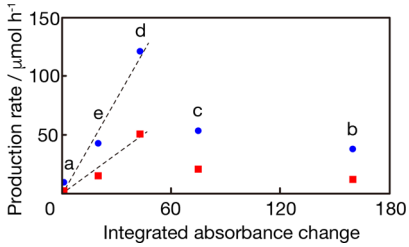

Figure 10. H_2 and O_2 production rate of the flux-prepared photocatalysts. H_2 (circles) and O_2 (squares) production rates are plotted as a function of integrated IR absorbance change in the unit of the absorbance change on Sr-free NTO: (a) Sr-free NTO, (b) 1h-Sr-NTO, (c) 10h-Sr-NTO, (d) 20h-Sr-NTO, and (e) 60h-Sr-NTO. The broken lines are for eye guidance.

DOI: 10.1021/acscatal.8b02437
ACS Catal. 2018, 8, 9334−9341

integrated absorbance change, as depicted with broken lines in the figure. The proportional relation suggests electron-to-H_2 conversion efficiency and hole-to-O_2 conversion efficiency insensitive to immersion time in the range of 20−60 h. 20h-Sr-NTO split more water than 60h-Sr-NTO, simply because more electrons and holes were present in the former than in the latter.

This proportional relation broke down with 10h-Sr-NTO and especially with 1h-Sr-NTO. These two photocatalysts produced H_2 and O_2 less than expected on the broken lines. Electron-to-H_2 and hole-to-O_2 conversion efficiency decreased by reducing immersion time in the order of 20, 10, and 1 h. The decreased conversion efficiency should be ascribed to surface accumulation of Sr cations caused by curtailed heating.

The Sr-accumulated layer capping the photocatalyst particles increased charge carrier concentration, but not necessarily leading to higher water splitting rates. The highest rates were achieved on 20h-Sr-NTO with a moderate gradient of Sr concentration.

A possible band diagram of 1h-, 20h- and 60h-Sr-NTO under the reaction condition is drawn in Figure 11. In 1h-Sr-NTO, photoexcited electrons are driven into the bulk by energy gradient of the conduction-band minimum. They are, on the other hand, required to return to the surface to contribute to the desired reaction. When the upward shift of the conduction band is large enough relative to thermal energy at room temperature, 25 meV, a major portion of electrons remain in the bulk so as not to contribute to the reaction on the surface.

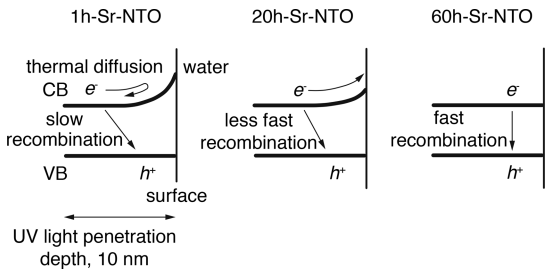

Figure 11. Band diagram of the Sr-NTO photocatalysts in water. CB: conduction band. VB: valence band.

In 20h-Sr-NTO with a small but finite gradient, excited electrons are still driven to be separated from holes. The upward conduction-band shift is not enough to repel the electrons from the surface, nevertheless. The number of electrons at the surface is consequently maximized in the series of Sr-NTO photocatalysts examined in this study.

In 60h-Sr-NTO, the homogeneous Sr distribution provides no energy gradient of the conduction-band minimum. Excited electrons quickly recombine with complementary holes.

On the flux-prepared Sr-NTO photocatalyst, H_2/O_2 molar ratio, which should be 2 in the stoichiometric splitting reaction, was 3.0−2.4 as summarized in Table 1. Consider origins of the observed deviations from the stoichiometry, less O_2 production than expected. Hole-consuming reactions to oxidize organic compounds contaminating the photocatalyst surface is always possible. The contribution of the undesired side reactions can be relatively enhanced when the rate of water splitting reaction is limited on 1h- and 60h-Sr-NTO as was observed. Partial oxidation of water to produce hydrogen peroxide provides another explanation. Water oxidation to O_2 requires four holes. A limited number of available holes is favorable for the partial oxidation rather than the full oxidation to O_2. The Sr-rich surface of the photocatalysts may be a poor catalyst for the full oxidation of water.

4. CONCLUSIONS

$NaTaO_3$ photocatalysts were doped with Sr cations through crystallization in NaCl flux heated at 1423 K. Particles of $NaTaO_3$−$Sr(Sr_{1/3}Ta_{2/3})O_3$ solid solution were obtained. Intraparticle distribution of Sr cations was sensitive to immersion time in the hot flux with a fixed Sr concentration of 2 mol % relative to Ta. Extended immersion for 60 h resulted in the homogeneous Sr distribution in each particle. Curtailed immersion for 1 h produced a 3 nm thick Sr-accumulated layer capping the particles. The population of bandgap-excited electrons under Hg−Xe lamp irradiation increased with decreasing immersion time, i.e., the largest population (160 times enhancement relative to the population in Sr-free $NaTaO_3$) in the 1-h immersed photocatalyst and the smallest population (9 times enhancement) in the 60-h immersed photocatalyst. We proposed an explanation for the significant population enhancement in the 1-h immersed photocatalyst with the concentration gradient of Sr cations from the surface to bulk. The concentration gradient induced an energy gradient of conduction-band minimum. Photoexcited electrons were driven along the energy gradient to be separated from holes. The overall water splitting reaction rate was enhanced by 4 times on the 1-h immersed photocatalyst relative to the rate on the Sr-free $NaTaO_3$. The reaction-rate enhancement less than the electron population enhancement was ascribed to a limited fraction of electrons overriding the energy gradient returning on the surface. Here we learned that creating Sr concentration gradient in photocatalyst particles had a double purpose: the total electron population increased, and their fraction to contribute surface reactions decreased. Optimizing the double edges of doping is required for rational design of semiconductor photocatalysts highly efficient for artificial photosynthesis.

■ ASSOCIATED CONTENT

Supporting Information

The Supporting Information is available free of charge on the ACS Publications website at DOI: 10.1021/acscatal.8b02437.

STEM and XANES results (PDF)

■ AUTHOR INFORMATION

Corresponding Author

*(H.O.) E-mail: oni@kobe-u.ac.jp.

ORCID

Mitsunori Kitta: 0000-0001-9800-7371
Akihide Iwase: 0000-0002-6395-9556
Hiroshi Onishi: 0000-0003-1873-9105

Notes

The authors declare no competing financial interest.

■ ACKNOWLEDGMENTS

Hidenori Saito of Kanagawa Academy of Science and Technology operated the scanning electron microscope. X-ray absorption measurements were performed under the approval of the Photon Factory Program Advisory Committee

DOI: 10.1021/acscatal.8b02437
ACS Catal. 2018, 8, 9334−9341

(Proposal No. 2016G057). This study was supported by JSPS KAKENHI Grant No. JP16H02250.

REFERENCES

(1) Yi, Z. G.; Ye, J. H. Band Gap Tuning of $Na_{1-x}La_xTa_{1-x}Co_xO_3$ Solid Solutions for Visible Light Photocatalysis. *Appl. Phys. Lett.* **2007**, *91*, 254108.

(2) Yi, Z. G.; Ye, J. H. Band Gap Tuning of $Na_{1-x}La_xTa_{1-x}Cr_xO_3$ for H_2 Generation from Water under Visible Light Irradiation. *J. Appl. Phys.* **2009**, *106*, 074910.

(3) Yang, M.; Huang, X.; Yan, S.; Li, Z.; Yu, T.; Zou, Z. Improved Hydrogen Evolution Activities under Visible Light Irradiation over $NaTaO_3$ Codoped with Lanthanum and Chromium. *Mater. Chem. Phys.* **2010**, *121*, 506−510.

(4) Matoba, T.; Maeda, K.; Domen, K. Activation of $BaTaO_2N$ Photocatalyst for Enhanced Non-Sacrificial Hydrogen Evolution from Water under Visible Light by Forming a Solid Solution with $BaZrO_3$. *Chem. - Eur. J.* **2011**, *17*, 14731−14735.

(5) Zhao, Z.; Li, R.; Li, Z.; Zou, Z. Photocatalytic Activity of La-N-Codoped $NaTaO_3$ for H_2 Evolution from Water under Visible-Light Irradiation. *J. Phys. D: Appl. Phys.* **2011**, *44*, 165401.

(6) Kanhere, P.; Nisar, J.; Tang, Y.; Pathak, B.; Ahuja, R.; Zheng, J.; Chen, Z. Electronic Structure, Optical Properties, and Photocatalytic Activities of $LaFeO_3$-$NaTaO_3$ Solid Solution. *J. Phys. Chem. C* **2012**, *116*, 22767−22773.

(7) Maeda, K.; Domen, K. Water Oxidation Using a Particulate $BaZrO_3$-$BaTaO_2$ N Solid-Solution Photocatalyst That Operates under a Wide Range of Visible Light. *Angew. Chem., Int. Ed.* **2012**, *51*, 9865−9869.

(8) Maeda, K.; Domen, K. ; et al. Preparation of $BaZrO_3$-$BaTaO_2N$ Solid Solutions and the Photocatalytic Activities for Water Reduction and Oxidation under Visible Light. *J. Catal.* **2014**, *310*, 67−74.

(9) Pan, C.; Takata, T.; Nakabayashi, M.; Matsumoto, T.; Shibata, N.; Ikuhara, Y.; Domen, K. A Complex Perovskite-Type Oxynitride: The First Photocatalyst for Water Splitting Operable at up to 600 nm. *Angew. Chem., Int. Ed.* **2015**, *54*, 2955−2959.

(10) Kudo, A.; Kato, H. Effect of Lanthanide-Doping into $NaTaO_3$ Photocatalysts for Efficient Water Splitting. *Chem. Phys. Lett.* **2000**, *331*, 373−377.

(11) Kato, H.; Asakura, K.; Kudo, A. Highly Efficient Water Splitting into H_2 and O_2 over Lanthanum-Doped $NaTaO_3$ Photocatalysts with High Crystallinity and Surface Nanostructure. *J. Am. Chem. Soc.* **2003**, *125*, 3082−3089.

(12) Iwase, A.; Kato, H.; Okutomi, H.; Kudo, A. Formation of Surface Nano-Step Structures and Improvement of Photocatalytic Activities of $NaTaO_3$ by Doping of Alkaline Earth Metal Ions. *Chem. Lett.* **2004**, *33*, 1260−1261.

(13) Kudo, A.; Niishiro, R.; Iwase, A.; Kato, H. Effects of Doping of Metal Cations on Morphology, Activity, and Visible Light Response of Photocatalysts. *Chem. Phys.* **2007**, *339*, 104−110.

(14) Iwase, A.; Kato, H.; Kudo, A. The Effect of Alkaline Earth Metal Ion Dopants on Photocatalytic Water Splitting by $NaTaO_3$ Powder. *ChemSusChem* **2009**, *2*, 873−877.

(15) Yamakata, A.; Ishibashi, T.; Kato, H.; Kudo, A.; Onishi, H. Photodynamics of $NaTaO_3$ Catalysts for Efficient Water Splitting. *J. Phys. Chem. B* **2003**, *107*, 14383−14387.

(16) Maruyama, M.; Iwase, A.; Kato, H.; Kudo, A.; Onishi, H. Time-Resolved Infrared Absorption Study of $NaTaO_3$ Photocatalysts Doped with Alkali Earth Metals. *J. Phys. Chem. C* **2009**, *113*, 13918−13923.

(17) An, L.; Onishi, H. Electron−Hole Recombination Controlled by Metal Doping Sites in $NaTaO_3$ Photocatalysts. *ACS Catal.* **2015**, *5*, 3196−3206.

(18) An, L.; Park, Y.; Sohn, Y.; Onishi, H. Effect of Etching on Electron-Hole Recombination in Sr-Doped $NaTaO_3$ Photocatalysts. *J. Phys. Chem. C* **2015**, *119*, 28440−28447.

(19) An, L.; Sasaki, T.; Weidler, P. G.; Wöll, C.; Ichikuni, N.; Onishi, H. Local Environment of Strontium Cations Activating $NaTaO_3$ Photocatalysts. *ACS Catal.* **2018**, *8*, 880−885.

(20) Porob, D. G.; Maggard, P. A. Flux Syntheses of La-Doped $NaTaO_3$ and Its Photocatalytic Activity. *J. Solid State Chem.* **2006**, *179*, 1727−1732.

(21) Lee, S.; Teshima, K.; Mizuno, Y.; Yubuta, K.; Shishido, T.; Endo, M.; Oishi, S. Growth of Well-Developed Sodium Tantalate Crystals from a Sodium Chloride Flux. *CrystEngComm* **2010**, *12*, 2871.

(22) Sun, J.; Chen, G.; Li, Y.; Jin, R.; Wang, Q.; Pei, J. Novel (Na, K)TaO_3 Single Crystal Nanocubes: Molten Salt Synthesis, Invariable Energy Level Doping and Excellent Photocatalytic Performance. *Energy Environ. Sci.* **2011**, *4*, 4052.

(23) Hojamberdiev, M.; Yubuta, K.; Vequizo, J. J. M.; Yamakata, A.; Oishi, S.; Domen, K.; Teshima, K. NH_3-Assisted Flux Growth of Cube-like $BaTaO_2$ N Submicron Crystals in a Completely Ionized Nonaqueous High-Temperature Solution and Their Water Splitting Activity. *Cryst. Growth Des.* **2015**, *15*, 4663−4671.

(24) Wang, S.; Xu, X.; Luo, H.; Bai, Y.; Abbas, S.; Zhang, J.; Zhao, J.; Tang, C. Enhanced Organic Dye Removal of the W and N Co-Doped $NaTaO_3$ under Visible Light Irradiation. *J. Alloys Compd.* **2016**, *681*, 225−232.

(25) Yamamoto, A.; Mizuba, S.; Saeki, Y.; Yoshida, H. Platinum Loaded Sodium Tantalate Photocatalysts Prepared by a Flux Method for Photocatalytic Steam Reforming of Methane. *Appl. Catal., A* **2016**, *521*, 125−132.

(26) Hulliger, J.; Gutmann, R.; Wägli, P. Growth of Monocrystalline Thin Films of Potassium-Tantalate-Niobate (KTN) by Liquid-Phase Epitaxy. *Thin Solid Films* **1989**, *175*, 201−206.

(27) Suzuki, S.; Teshima, K.; Yubuta, K.; Ito, S.; Moriya, Y.; Takata, T.; Shishido, T.; Domen, K.; Oishi, S. Direct Fabrication and Nitridation of a High-Quality $NaTaO_3$ Crystal Layer onto a Tantalum Substrate. *CrystEngComm* **2012**, *14*, 7178.

(28) Ahtee, M.; Unonius, L. The structure of $NaTaO_3$ by X-ray powder diffraction. *Acta Crystallogr., Sect. A: Cryst. Phys., Diffr., Theor. Gen. Crystallogr.* **1977**, *33*, 150−154.

(29) Shannon, R. D. Revised Effective Ionic Radii and Systematic Studies of Interatomic Distances in Halides and Chalcogenides. *Acta Crystallogr., Sect. A: Cryst. Phys., Diffr., Theor. Gen. Crystallogr.* **1976**, *32*, 751−767.

(30) In *CRC Handbook of Chemistry and Physics*, 92nd ed.; Haynes, W. M., Lide, D. R.,, Eds.; CRC Press: Boca Raton, FL, 2011; pp 4-91−4-93.

(31) Lee, W. Y.; Bae, Y. W.; Stinton, D. E. Na_2SO_4-Induced Corrosion of Si_3N_4 Coated with Chemically Vapor Deposited Ta_2O_5. *J. Am. Ceram. Soc.* **1995**, *78*, 1927−1930.

(32) Teixeira, N. G.; Dias, A.; Moreira, R. L. Raman Scattering Study of the High Temperature Phase Transitions of $NaTaO_3$. *J. Eur. Ceram. Soc.* **2007**, *27*, 3683−3686.

(33) Ikeda, T.; Fujiyoshi, S.; Kato, H.; Kudo, A.; Onishi, H. Time-Resolved Infrared Spectroscopy of $K_3Ta_3B_2O_{12}$ Photocatalysts for Water Splitting. *J. Phys. Chem. B* **2006**, *110*, 7883−7886.

(34) Lewis, N. S.; Rosenbluth, M. L. Theory of Semiconductor Materials. In *Photocatalysis, Fundamentals and Applications*; Serpone, N., Pelizzeti, E., Eds.; John Wiley and Sons: New York, 1989; pp 60−62 and Figure 3.8.

DOI: 10.1021/acscatal.8b02437
ACS Catal. 2018, 8, 9334−9341